IET Research Journals

Submission Template for IET Research Journal Papers

IET Journals
The Institution of Engineering and Technology

SISAR Imaging for Space Debris based on Nanosatellites

ISSN 1751-8644
doi: 0000000000
www.ietdl.org

Ilias Theodorou[1], *Christos Ilioudis*[1], *Carmine Clemente*[1], *Massimiliano Vasile*[2], *John Soraghan*[1]

[1] *Department of Electronic & Electrical Engineering, University of Strathclyde, Glasgow, United Kingdom*
[2] *Department of Mechanical & Aerospace Engineering, University of Strathclyde, Glasgow, United Kingdom*
* *E-mail: ilias.theodorou@strath.ac.uk*

Abstract: The increasing amount of space debris poses a growing challenge in the development of space travel. In previous work, a proposed system comprising of a low budget space-borne passive radar based on CubeSAT, flying in Low Earth Orbit (LEO), demonstrated promising results in terms of space debris detection performance. In this work a novel Shadow ISAR (SISAR) model for space debris imaging based on nanosatellite is presented. An analysis of the received Forward Scattering (FS) signal is provided along with a novel model for moving transmitters and receivers SISAR imaging. Using simulated data and assuming different scenarios the performance of the new algorithm is assessed wherein, a classification scheme is applied using the output of the SISAR algorithm for classification between simple target shapes.

1 Introduction

Since Sputnik 1, space activities over the subsequent decades have resulted in a significant amount of space debris. The degree of space debris, with unknown behavior, pose increasing risk to existing and future space missions. This has made space traffic management extremely challenging. Typical space debris orbital velocities (around 26000 km/h in LEO) are high enough, even for small orbital debris, to allow them to damage any active satellite or spacecraft. Old inactive satellites, disgraded upper stages and fragments from space collisions and explosions constitute the main population of space debris [1, 2]. Collisions between space objects will result in even more "space junk" that will create a cascade, known as the Kessler syndrome, according to NASA [3]. Nowadays many systems are designed for the problem of providing data measurements to detect and track down these space objects for better space traffic monitoring.

In 2009 the European Space Agency (ESA) initiated a program known as Space Situational Awareness (SSA), where one of its main component comprised a space surveillance and tracking (SST) segment, which aimed to detect and catalog active and inactive satellites and space debris [4]. Both radar and optical sensors are used for detecting and tracking space debris objects. The European Incoherent Scatter Scientific Association (EISCAT) exploits three existing radar systems, used for atmosphere and ionosphere studies, to track space debris in LEO down to 2cm in size [5]. The Tracking and Imaging Radar (TIRA), is a space observation radar located at the Fraunhofer Institute for High Frequency and Physics and Radar Techniques in Germany. This system, is equipped with a 34m dish antenna operating in L-band and can detect and calculate coarse orbit information for space objects down to few centimeters at 1000km of altitude [6]. However, ground-based systems may have limitations related to long distances to the targets as well as atmosphere and weather related signal attenuations. Furthermore, the cost of the large antennae and the transmission power needed may be considered relatively high compared to the achieved performance. For these reasons, alternative solutions exploiting illuminators of opportunity are attractive.

The concept of using passive radar to address the SSA monitoring was proposed by Benson in 2014 [7]. This work reported on the detection performance of a ground-based passive system using as illuminator of opportunity the Global Navigation Satellites and introduced methods for improving the weak scattered signals coming from space debris. Inspired by [7] in our earlier work [8], we proposed a novel system for space debris detection tracking and characterization. The system consists of a passive space-borne radar installed on one or more nanosatellites flying in LEO. Exploiting any RF source signals coming from higher altitude illuminators, the system can detect, track and characterize space objects in both bistatic and forward scattering mode. The main motivation for this passive space-borne system is that it overcomes the atmospheric losses and reduces the distance between transmitter and receiver. Also, this proposed system benefits from current sensors in terms of cost, spatial and temporal coverage. As shown in [8], due to the lower relative velocities between the transmitter and receiver, integration time can be significantly enhanced and thus detection performance is increased. The orbital parameters of such a system can be dynamically chosen providing spatial coverage at specific altitudes of interest. Furthermore, specific illuminators of opportunity for best output performance are available. The proposed system is considered to be cost efficient compared with existing sensors which are operating in active mode using large ground-based antennas and high transmission power. In [9], the detection performance was assessed on simulated data showing that the system would be able to detect space objects down to a few centimeters in size. Various algorithms such as 2D and 3D imaging exploiting inverse synthetic aperture radar (ISAR) techniques have been reported that demonstrate space object characterization [10–15].

In this paper, Shadow Inverse Synthetic Aperture Radar (SISAR) is investigated for space debris detection and characterization exploited from a nanosatellite based passive radar. SISAR was first introduced by Chapurskiy in the 1980s [16]. The principle of SISAR is that the FS signal in the Fresnel zone can be expressed as the Fresnel transform of the target's complex profile function (CPF), from which information about the target contour can be extracted. A novel signal model for moving transmitter moving receiver was first introduced in [17], which can be used to fit more complex scenarios such as in the case of passive space-borne radar based on nanosatellite systems. The moving-end (ME) SISAR algorithm [17], can be considered as a generalisation of the classic SISAR algorithm, which in this case is modified to fit the problem of space debris detection and characterisation from nanosatellite. The output of the SISAR algorithm is very similar to the target contour and thus, it can be used directly as a feature to feed a classifier that could be used for enhanced space debris tracking. In this work, after the derivation of the ME-SISAR imaging for space debris, the capabilities to exploit the extracted profiles for target classification are assessed using a k-NN classifier.

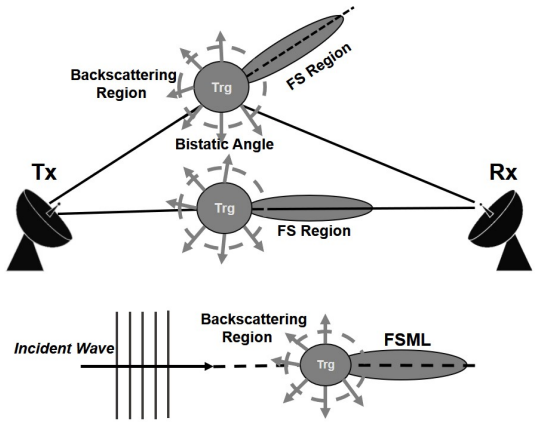

Fig. 1: Forward Scattering geometry

The remainder of the paper is organized as follows. Section 2 describes the Forward Scattering Radar concept. Section 3 introduces the new SISAR model for moving-ends as well as the space object geometry. In Section 4, a power budget analysis is presented whereas, simulation results are presented in Section 5 followed by conclusions in Section 6.

2 Forward Scattering Radar

Forward Scattering Radar (FSR), is a special bistatic radar configuration occurring when the bistatic angle is close to 180^o[18]. The concept of FSR is illustrated in Fig. 1. The transmitter and receiver are spatially separated and facing each other on a baseline. According to Babinet's principle, the signal diffracted around a target of a given silhouette area will be equal and opposite to that diffracted through an equivalent target-shaped hole in an infinite screen perpendicular to the path between transmitter and receiver [19]. As shown in Fig. 1, the FS region is in the forward direction of the line of sight between the transmitter and the target. The target is considered to fall into the FS region when the forward scattering main lobe (FSML) is within the receiver's beam. The main advantage of FSR, is that the radar cross section (RCS) enhancement in the FSML direction known as forward scattering cross section (FSCS), and it becomes maximum when the bistatic angle reaches 180^o [20]. Generally, all targets fall into three scattering regions known as, Rayleigh region ($D/\lambda << 1$), Mie region ($D/\lambda \approx 1$) and the Optical region ($D/\lambda >> 1$), where D is the typical target's dimension and λ the operating wavelength. FSCS is mainly increased in the optical region and the maximum value is given by:

$$\sigma_{FSmax} = \frac{4\pi U^2}{\lambda^2} \tag{1}$$

where U, is the silhouette area of the target. The FSML width depends on the target's size and is given by:

$$\theta_{FS} = \frac{\lambda}{D}\ [rad] \tag{2}$$

Fig. 2, demonstrates the normalised values of monostatic RCS, FSCS and FSML width size θ_{FS} of a sphere with diameter length D. From Fig. 2, it is clear that FSCS is significantly increased in the optical region. However, the FSML width is inversely proportional to the FSCS increase, leading to a trade off between target's reflectivity and the FS region [21].

3 Moving-Ends Shadow Inverse SAR

In this section the SISAR imaging algorithm is discussed and the generalized model based on the ME scenario is described. The

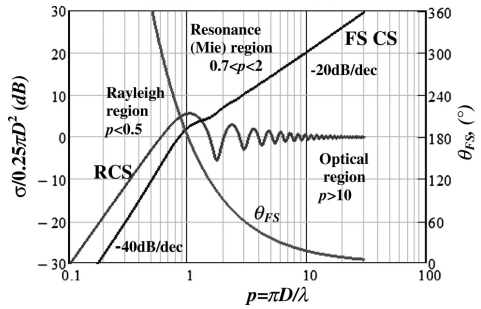

Fig. 2: RCS and FSML width of spherical target. [21]

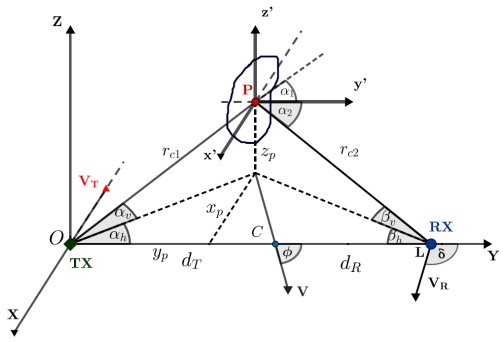

Fig. 3: FSR Topology

geometry of such a scenario is shown in Fig. 3. All system components (target, transmitter and receiver) are randomly moving in space with the target moving in a plane which is parallel to the XY plane and with an angle ϕ relative to the baseline, the receiver is moving with an angle δ in respect to the baseline whereas, the transmitter is moving along the X-axis. The coordinate system (x',y',z') is parallel to (X,Y,Z) system and its origin is located at the geometrical centre of the target with the target contour projection placed in the x'z' plane. The distance variables r_{c1} and r_{c2} are the distances from the transmitter and receiver to the target's centre respectively. At time t=0, all three components are aligned with the transmitter position at the origin of the (X,Y,Z) and the receiver located at (0,L,0) where L, is the distance variable for the baseline between transmitter and receiver. In the optical region, the received Forward Scattering (FS) signal received from a target can be expressed using Fresnel-Kirchhoff diffraction formula as [22]:

$$\dot{E}(t) = \frac{-jA}{2\lambda} \int\int \epsilon_\tau(x', z') \frac{e^{jk(r_1+r_2)}}{r_1 r_2} (\cos\alpha_1 + \cos\alpha_2)\, dx'\, dz' \tag{3}$$

where A is the transmitting signal amplitude, $k = 2\pi/\lambda$ and r_1, r_2 are the distances from the transmitting source to every point of the target's projected aperture and from that point to the receiver end respectively and α_1, α_2 are the diffraction angles. The values of r_1 and r_2 can be calculated as:

$$r_1 = \sqrt{\Big([X_{Tx}(t) - (X_p(t) + x')]^2 + [Y_{Tx}(t) - (Y_p(t) + y')]^2 + [Z_{Tx}(t) - (Z_p(t) + z')]^2\Big)} \tag{4}$$

$$r_2 = \sqrt{\Big([X_{Rx}(t) - (X_p(t) + x')]^2 + [Y_{Rx}(t) - (Y_p(t) + y')]^2 + [Z_{Rx}(t) - (Z_p(t) + z')]^2\Big)} \tag{5}$$

where $(X\text{-}Y\text{-}Z)\big|_{Tx/Rx/p}$ are the transmitter/receiver/target coordinates in time. Additionally, ϵ_τ is the indicator function of the

shadow profile of the target S.

$$\epsilon_\tau = \begin{cases} 1, & (x', z') \in S \\ 0, & (x', z') \notin S \end{cases}$$

Under the assumptions that the target is moving near the baseline in both X and Z directions and that the baseline length is not comparable with the target's size, the two distance variables from (4) and (5) can be approximated as:

$$r_1 \approx r_{c1} + \frac{x'^2 + 2x'\,[X_p(t) - X_{Tx}(t)] + z'^2 + 2z'[Z_p(t) - Z_{Tx}(t)]}{2r_{c1}} \tag{6}$$

$$r_2 \approx r_{c2} + \frac{x'^2 + 2x'[X_p(t) - X_{Rx}(t)] + z'^2 + 2z'[Z_p(t) - Z_{Rx}(t)]}{2r_{c2}} \tag{7}$$

and the sum of cosines of the diffraction angles from (3):

$$cos\alpha_1 + cos\alpha_2 \approx 2 \tag{8}$$

assuming α_1 and α_2 are close to zero. Using (6), (7) and (3) the FS signal for SISAR can be derived as:

$$\dot{E}(t) = \frac{A\exp\left[jk(r_{c1}+r_{c2})\right]}{j\lambda r_{c1}r_{c2}} \int_S \dot{H}(x') \exp\left[jkx'^2\left(\frac{1}{2r_{c1}} + \frac{1}{2r_{c2}}\right)\right] \exp\left[jkx'\left(\frac{X_p(t) - X_{Tx}(t)}{r_{c1}} + \frac{X_p(t) - X_{Rx}(t)}{r_{c2}}\right)\right] dx' \tag{9}$$

The function $\dot{H}(x')$ is the complex profile function of the target and is defined as:

$$\dot{H}(x') = \int \epsilon(x', z') \exp\left[jkz'^2\left(\frac{1}{2r_{c1}} + \frac{1}{2r_{c2}}\right)\right] \exp\left[jkz'\left(\frac{Z_p(t) - Z_{Tx}(t)}{r_{c1}} + \frac{Z_p(t) - Z_{Rx}(t)}{r_{c2}}\right)\right] dz' \tag{10}$$

In order to understand how to set the limits of the integral let us introduce a target profile example in Fig 4. The two parameters $h(x')$ and $m(x')$ are the height difference and the median line of the target and are related as:

$$m(x') = \frac{h(x')}{2} \tag{11}$$

Therefore, one can see that the limits for the CPF integral in the z' direction, can be set by replacing the indicator function ϵ_τ, with limits from $[0\,, h(x')]$ or for convenience with the calculations, from $\left[m(x') - \frac{h(x')}{2},\ m(x') + \frac{h(x')}{2}\right]$ as:

$$\dot{H}(x') = \int_{m(x')-\frac{h(x')}{2}}^{m(x')+\frac{h(x')}{2}} \exp\left[jkz'^2\left(\frac{1}{2r_{c1}} + \frac{1}{2r_{c2}}\right)\right] \exp\left[jkz'\left(\frac{Z_p(t) - Z_{Tx}(t)}{r_{c1}} + \frac{Z_p(t) - Z_{Rx}(t)}{r_{c2}}\right)\right] dz' \tag{12}$$

and by ignoring the second order variation of z' and carrying out the integral, the CPF can be approximated as:

$$\dot{H}(x') \approx h(x')\,\mathrm{sinc}\left[k\,h(x')\left(\frac{Z_p(t) - Z_{Tx}(t)}{2r_{c1}} + \frac{Z_p(t) - Z_{Rx}(t)}{2r_{c2}}\right)\right] \exp\left[jk\,m(x')\left(\frac{Z_p(t) - Z_{Tx}(t)}{r_{c1}} + \frac{Z_p(t) - Z_{Rx}(t)}{r_{c2}}\right)\right] \tag{13}$$

According to (13), the magnitude and the phase of the CPF can provide the height difference and median line respectively, where the sinc term in the magnitude can be approximated very close to 1 since the target is moving near the baseline and thus, the Z coordinate difference between the objects is very small compared to the two variables r_{c1} and r_{c2} inside the sinc argument in (13).

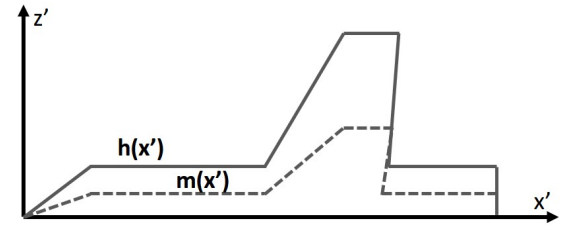

Fig. 4: Target profile

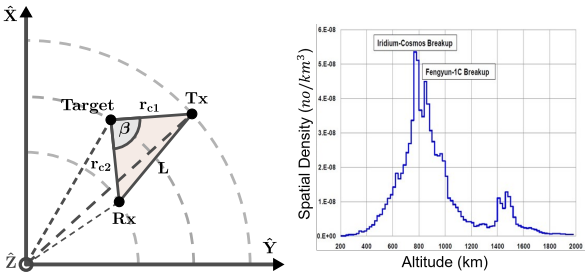

(a) Space Geometry (b) Spatial Density of Space object, (source: Nasa 2011 [23])

Fig. 5: (a) Space Geometry (b) Space Object spatial density

3.1 Space Geometry

The topologyof the space geometry is illustrated in Fig. 5a. The origin of the coordinate system ($\hat{X}$,$\hat{Y}$,$\hat{Z}$) is the Earth's geometrical centre. Circular orbits are considered for simplicity for all space objects (Tx,Rx and targets). At time *t*=0, Tx, Rx and target are aligned and located on the Y-axis resulting a bistatic angle β = 180^o. The position vector for a space object in circular orbit can be estimated as follow:

$$P_{obj}(t) = \begin{bmatrix} X(t) \\ Y(t) \\ Z(t) \end{bmatrix} = R_{obj} \begin{bmatrix} \sin(\omega_{obj}t)\cos(\alpha_{\mathrm{obj}}) \\ \cos(\omega_{obj}t) \\ \sin(\omega_{obj}t)\sin(\alpha_{\mathrm{obj}}) \end{bmatrix} \tag{14}$$

where the *obj* subscript refers to any space object between Tx, Rx and target. The variable R_{obj} denotes the altitude of any space object from the Earth's centre and the angle α_{obj} is the inclination angle of the object's orbit from the reference circular orbit in the XY plane. The variable ω_{obj} is the angular velocity of any space object defined as:

$$\omega_{obj} = \sqrt{\frac{\mu}{\mathrm{R}_{\mathrm{obj}}^3}}\ [rad/s] \tag{15}$$

where μ is the standard gravitational parameter of the Earth and is equal $\mu \approx 3.99 \times 10^{14}\ \frac{m^3}{s^2}$.

3.2 Observation Time

The importance of the total observation time is discussed in this section. Both detection performance, in terms of the target size, and SISAR resolution are highly depended on the observation time which is significantly enhanced due to the lower relative velocities introduced from the receiver since it is in orbit. In general, observation time depends on the total time that the targets is within FS region [21]. This means that the physical size of the target and the FSML width, determines the maximum observation time which can be estimated using the condition:

$$\beta \geq 180^o - \frac{\theta_{FS}^o}{2} \tag{16}$$

Table 1 Link Budget Parameters

Parameter	Description		HY2A	GSTAR	Jason-3
G_r	Receiver antenna Gain	[dB]	37.65	23	30
EIRP	Effective radiated power	[dB]	53	37	56
BW	Radar Bandwidth	[MHz]	320	16.5	320
G_{sp}	Signal Processing gain	[dB]	45.15	52.17	45.28
G_{LNA}	LNA gain	[dB]	40	50	40
F	Radar noise figure	[dB]	10	12	10
Altitude	Satellite altitude	[km]	963	1400	1336
D_a	Receiver antenna diameter	[m]		0.6	
k_0	Boltzmann constant	[J/K]		1.38×10^{-23}	
T_0	Noise reference temperature	[K]		290	
SNR	Signal-to-Noise ratio at receiver	[dB]		10	
L_s	Loss factor	[dB]		1	

From Fig. 5a, the bistatic angle β can be calculated as:

$$\beta = \cos^{-1}\left(\frac{r_{c1}^2 + r_{c2}^2 - L^2}{2r_{c1}r_{c2}}\right) \tag{17}$$

where the distance variables in (17), can be expressed using the geometry in Fig. 5a as:

$$\begin{aligned} r_{c1} &= ||P_{Tx}(t) - P_p(t)|| \\ r_{c2} &= ||P_{Rx}(t) - P_p(t)|| \\ L &= ||P_{Rx}(t) - P_{Tx}(t)|| \end{aligned} \tag{18}$$

According to (2), the FSML width is a function of the target's length. The observation time can be evaluated assuming the worst case scenario in terms of the relative motion between space objects. Therefore, by setting the inclination angle of the receiver and the target with π rads of difference, the two orbits will be coplanar with opposite direction. The maximum target length considered for this analysis is 2m, and the nanosatellite is fixed at 400km. The target altitude range of focus can be seen from Fig. 5b, which shows the spatial density of space objects in LEO, where a noticable concentration is around 800km [23] and thus for this analysis the target altitude range is set between [700km - 900km].

For the analysis three different satellites are investigated as illuminators. The first one is the Haiyang-2A (HY2A) which is an ocean observation satellite approved by China National Space Administration (CNSA). The HY2A is equipped with an active radio altimeter, operating in dual-frequency (Ku, C-band) creating chirps with bandwidths 320MHz at Ku-band and 160MHz at C-band [24]. The second illuminator is the Jason-3 satellite developed for ocean height measurement. This satellite is equipped with the Poseidon-3B altimeter, which is a dual-frequency (5.3 and 13.6 GHz) radar altimeter [25]. The last illuminator of opportunity considered, is the Global Star constellation. This satellite operation is for satellite phone and low-speed data communications and is set to an altitude of 1400km [26]. The operating band for broadcasting is C-to-S band. Table 1, shows the parameters for all three satellites. For all three illuminators and all target altitudes in the focusing range, the bistatic angle is evaluated as a function of time and by varying the targets physical length, the total time is evaluated where the condition in (16) is satisfied. This total time can be considered as the maximum observation time from the receiver. Fig. 6, shows the maximum observation time in seconds, where a target is within FS region for different target altitudes. For all target's length and for three different satellites, it is safe to assume at least 1s of observation time, whereas for smaller targets of less than 1m length, observation time can reach up to 2-6 seconds. It is worth noting that these assumptions are made considering the worst case scenario in terms of observation time. For inclination angles less than π rads the observation time can reach much higher values since relative velocities are decreased.

3.3 SISAR Signal Model for Space Debris

In this system, the nanosatellite is considered to be the lowest flying space object at around [300km-600km] and therefore is considered to be the fastest component of the system compared to both

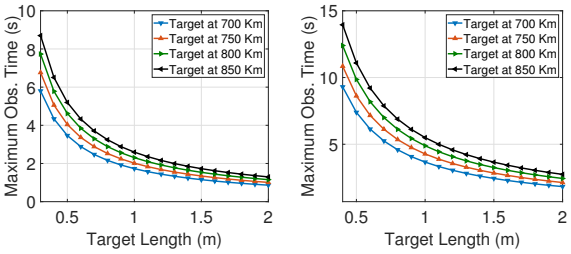

(a) HY2A (b) Jason 3

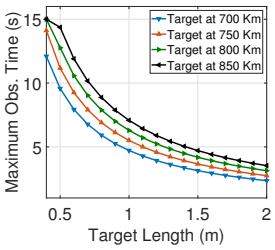

(c) GSTAR

Fig. 6: Maximum observation time in terms of target length

the higher altitude illuminator and target. Therefore, the maximum angular velocity can be estimated using (15) and setting the sensor at 300km of altitude as:

$$\omega_{max} = \sqrt{\frac{\mu}{R_{min}^3}} \approx 0.066 \text{ [deg/s]} \tag{19}$$

From (19) and Fig. 6, one can see that the argument $(\omega_{obj}t)$ in the position vector in (14), may be considered to be small enough to use small angle approximation. Thus, the position vector in (14) can be approximated as:

$$P_{obj}(t) = \begin{bmatrix} X(t) \\ Y(t) \\ Z(t) \end{bmatrix} \approx R_{obj} \begin{bmatrix} \omega_{obj}\cos(\alpha_{\text{obj}})\, t \\ 1 - \frac{(\omega_{obj}t)^2}{2} \\ \omega_{obj}\sin(\alpha_{\text{obj}})\, t \end{bmatrix} \tag{20}$$

Using (9), and the position vector approximation in (20), the time domain received signal for space geometry shown in Fig. 5a can be expressed as:

$$\dot{E}(t) = \dot{Q}\int_S \dot{H}(x')\exp\left[j\eta x'^2\right]\exp\left[j\gamma x' t\right]dx' \tag{21}$$

where

$$\begin{aligned} \dot{Q} &= \frac{A\exp\left[jk(r_{c1}+r_{c2})\right]}{j\lambda r_{c1}r_{c2}}, \qquad \eta = k\left(\frac{1}{2r_{c1}} + \frac{1}{2r_{c2}}\right) \\ \gamma &= k\sqrt{\mu}\,\Gamma_p\left(\frac{1-\frac{\Gamma_{Tx}}{\Gamma_p}}{r_{c1}} + \frac{1-\frac{\Gamma_{Rx}}{\Gamma_p}}{r_{c2}}\right) \end{aligned} \tag{22}$$

with the parameter Γ_{obj} defined as:

$$\Gamma_{obj} = \frac{\cos(\alpha_{obj})}{\sqrt{R_{obj}}} \tag{23}$$

To extract the CPF, the inverse transformation with respect to (21)

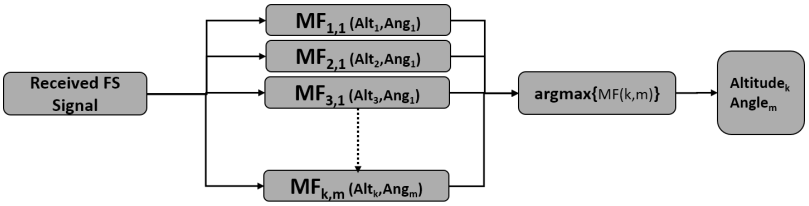

Fig. 7: Processing Diagram

has to be applied on the received signal. Assuming that both transmitter and receiver motion trajectories are known, the target's motion parameters (altitude and inclination angle) must be estimated before the CPF is extracted using the target motion estimation method shown in the next section. Therefore, CPF can be extracted as follow:

$$\dot{H}(x') = \frac{\gamma}{2\pi\dot{Q}} \exp\left[-j\eta x'^2\right] \int_T \dot{E}(t) \exp\left[-j\gamma x' t\right] dt \quad (24)$$

where γ must be estimated for target motion compensation.

3.4 Target motion parameters estimation:

Generally, the motion parameters of the target in a real scenario are unknown. Assuming both receiver and transmitter trajectories are known, the target's altitude and inclination angle must be estimated in order to perform SISAR imaging. A way to address this issue is with a bank of matched filters [27]. The received baseband signal is cross correlated with a bank of reference functions, created by varying both target altitude and inclination angle. A reference function for the cross correlation is in the form:

$$S_{ref}(t) = -W(t) \cdot [\sin(\psi(t)) + j\cos(\psi(t))] \quad (25)$$

where $W(t)$ is a window function, and the phase $\psi(t)$ is defined as:

$$\psi(t) = \frac{2\pi}{\lambda}(\hat{r}_{c1} + \hat{r}_{c2}) \quad (26)$$

where, $\hat{r}_{c1}(t)$ and $\hat{r}_{c1}(t)$, can be estimated using (18) for a range of target altitudes and inclination angles, [28, 29]. The maxima of the cross correlation output are evaluated using:

$$C_{out} = \left|IFFT\left\{FFT(S^*_{ref}) \cdot FFT(\dot{E})\right\}\right| \quad (27)$$

where * operator denotes the complex conjugate.
Fig. 7 shows the processing block diagram for target parameters estimation whereas, Fig. 8 shows the MF output C_{out} by varying both target altitude and inclination angle. The maximum peak provides the estimated target altitude and inclination angle. The accuracy of this technique depends on both signal to noise ratio SNR of the received signal as well as on how fine is the search grid for both inclination angle and altitude. In all cases shown in Fig. 8, the target orbital parameters (altitude and inclination angle), are successfully estimated and thus, the CPF of the target can be extracted. However, error in the estimation can cause distortion on the final image as well as size mismatch errors of the target. Furthermore, in Fig. 8 one can see the ambiguities arise. The received signal is passed through filters created by choosing a specific altitude and inclination angle for the target and therefore, it is possible that different combinations of target altitude and inclination angle may produce the same relative motion between target-receiver and/or target-transmitter and thus, a similar FS output signal with a high correlation factor. The computational complexity of this process can be estimated using (27). Three fast Fourier transforms of length L_n, which is the length in samples of the received signal are taking place meaning that $3L_n \log(L_n)$ operations are implemented. Furthermore, L_n operations are considered for the multiplication in the equation. This procedure is repeated

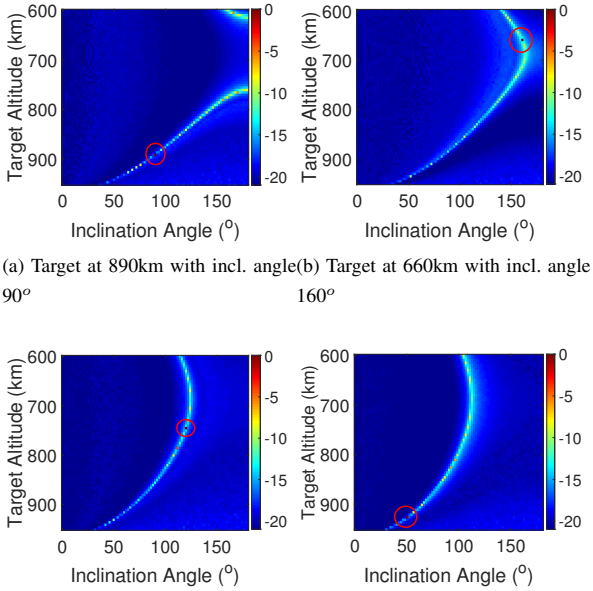

(a) Target at 890km with incl. angle 90^o (b) Target at 660km with incl. angle 160^o

(c) Target at 745km with incl. angle 120^o (d) Target at 925km with incl. angle 50^o

Fig. 8: Matched filter outputs for different system parameters.

over all the searching grid of size $m \times n$, which is defined from the size step of the focusing altitude and inclination angle ranges. The total computational complexity can be estimated as:

$$J = \left[3L_n \log(L_n) \times L_n\right] \times \frac{\Delta_R}{m_s} \times \frac{\Delta_\phi}{n_s} \quad (28)$$

where Δ_R and Δ_ϕ are the focusing altitude and inclination angle ranges and m_s and n_s are their corresponding altitude and angle step sizes.

3.5 SISAR Resolution

The resolution in SISAR imaging depends on the topology. The finer the resolution in the x' direction the smaller the target contour can be reconstructed. Using (24), the SISAR resolution can be estimated. The integral in (24), has a Fourier relation of the pair x' variable and time t. Therefore, the resolution $\delta x'$ can be estimated by relating the frequency resolution $\delta\omega = \frac{2\pi}{T_s}$ to the resolution in x' variable:

$$\begin{aligned} \omega &= \gamma x' \\ \delta\omega &= \gamma\, \delta x' \\ \delta x' &= \frac{2\pi}{T_s \gamma} \end{aligned} \quad (29)$$

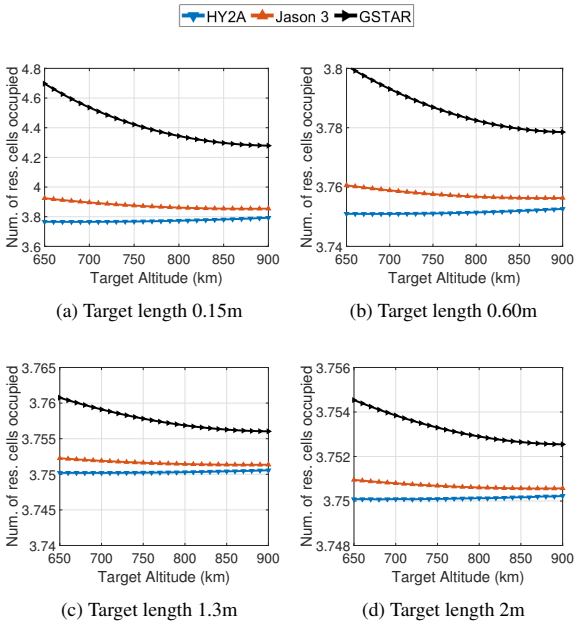

(a) Target length 0.15m (b) Target length 0.60m

(c) Target length 1.3m (d) Target length 2m

Fig. 9: Resolution cells occupied in terms of target size and altitude.

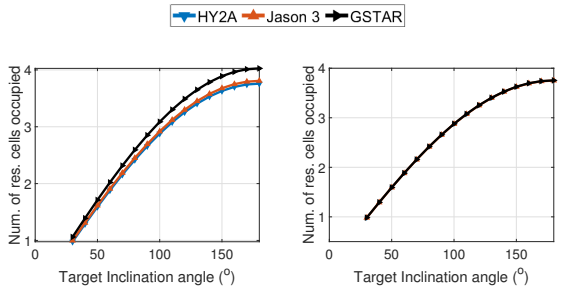

(a) Target length 0.2m (b) Target length 1.5m

Fig. 10: Resolution cells occupied in terms of target size and inclination angle.

where T_s is the observation time. To obtain the resolution in x' variable, the γ variable in (22) is substituted into (29) as:

$$\delta x' = \frac{\lambda\zeta(1-\zeta)L}{T_s\sqrt{\mu}\left[\Gamma_p - [\zeta\Gamma_{Tx} + (1-\zeta)\Gamma_{Rx}]\right]} \tag{30}$$

where ζ is a scale factor, $0 < \zeta < 1$, which expresses the crossing point C from Fig. 3 in terms of the baseline length L at the crossing time and it is defined as:

$$\zeta = \frac{d_R}{d_R + d_T} \tag{31}$$

where d_R and d_T, are the distance from the target's crossing point to the receiver and transmitter respectively (see Fig. 3). From (30), it can be seen that the resolution in SISAR depends on the baseline length, target's crossing point, total observation time and on the objects altitudes difference which ultimately maps to the relative velocities of the objects, as shown in (15). In Fig. 9, the acquired resolutions cells are plotted in terms of the target altitude and size. The receiver altitude is kept fixed at 400km whereas, depending on the target size and altitude, the observation time is calculated using the condition in (16) and therefore, the integration time is chosen dynamically. The inclination angle of the target is fixed at 180^o and the resolution cells are calculated by dividing the target's length over the variable δx. From Fig. 9, one can see that there is an inverse relation between target length and integration time since for smaller targets observation time increases due to the increase of the FSML and vice versa. Therefore, the target's altitude may not be considered as a major factor for the system resolution ability. The impact of inclination angle of the target is shown in Fig. 10. The receiver is fixed at 400km and target is flying exactly at the midpoint of the transmitter and the receiver. From Fig. 10, one can see that resolution is maximum when the target is moving in opposite direction of both receiver and transmitter due to the higher relative velocities and is getting worse while the inclination angle is getting lower. In this example, the target must be flying with an inclination angle of 100^o or higher in order to obtain minimum 3 resolution cells, which as will be shown later is a condition sufficient in order to provide a good correct classification rate. Therefore, the resolution of this algorithm is highly depended on the inclination angle between the target and the two ends and is not highly affected from target altitude with the assumption that integration time is dynamically chosen.

4 Power Budget

In this section a power budget analysis is presented. More specific, an investigation for the minimum detectable target size will be conducted in order to understand the detection capabilities of this system. The key performance metric for this assessment is the radar cross section of a target. Using radar range equation for the bistatic case, the signal-to-noise ration (SNR) at the receiver-end side can be estimated for a target at a specific altitude [19]:

$$SNR = \frac{P_t G_t G_r \sigma \lambda^2 L_s}{(4\pi)^3 r_{c1} r_{c2} P_n} \sqrt{N} G_{sp} \tag{32}$$

where P_t is the transmitting power, G_t is the transmitter's antenna gain, L_s $(0 < L_s \leq 1)$ is a loss factor including atmospheric, signal processing and other losses, N is defined as the total observation time and the term $\sqrt{N}$ defines that the integration is non-coherent. G_{sp} is known as the signal processing gain which is introduced after processing the received signal (e.g. matched filtering) and is defined by the product between the transmitted pulse duration and the transmitter bandwidth [19]. Finally, P_n is the noise power which is defined as: $P_n = k_0 T_0 B_r F$ with k_0 the Boltzman's constant, T_0 the noise reference temperature, F the receiver noise figure, and B_r is the bandwidth of the receiver. The receiver antenna could be either a high gain deployable parabolic dish or a foldable patch array [30–32]. In this analysis, a deployable parabolic antenna is considered and therefore the receiver antenna gain G_r can be calculated as:

$$G_r = \eta_e \left(\frac{\pi D_a}{\lambda}\right)^2 \tag{33}$$

where η_e and D_a are the antenna efficiency and antenna diameter respectively. For this paper the antenna efficiency η_e is set to 0.5 and

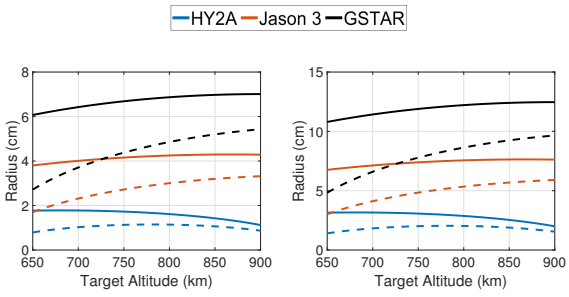

(a) SNR - 0dB (b) SNR - 10dB

Fig. 11: Minimum Detectable sphere radius: Solid line - receiver at 400km , Dashed line - receiver at 600km

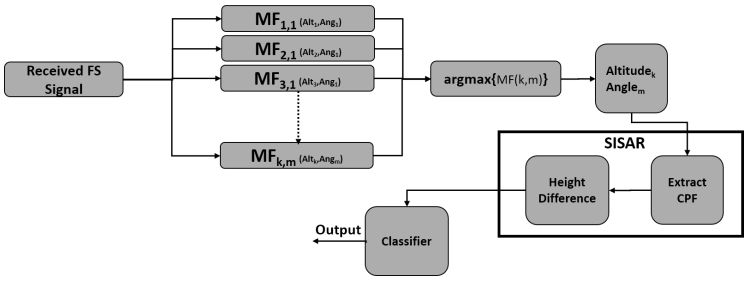

Fig. 12: System block diagram

the antenna diameter D_a equal to 0.6m.
From (32), the minimum detectable radar cross section RCS parameter σ_{min}, can be expressed as:

$$\sigma_{min} = \frac{(4\pi)^3 r_{c1} r_{c2} k_0 T_0 B_r F}{P_t G_t G_r \lambda^2 L_s G_{sp} \sqrt{N}} SNR \tag{34}$$

where SNR is a fixed value and the loss factor L_s is set to unity, as the atmospheric losses in such altitudes can be neglected. For simplicity sphere targets are considered for this analysis. From the FS theory the RCS of a perfect conducting sphere in FS depends only on the size and the operating wavelength and according to (1) can be evaluated as:

$$\sigma_{FS_{sphere}} = \frac{4\pi^3 \rho^4}{\lambda^2} \tag{35}$$

where the area variable U in (1), is replaced with the area of a projected circle with radius ρ. Therefore, using (34) and (35) the minimum detectable sphere radius can be estimated as:

$$\rho = \sqrt[4]{\frac{16\, r_{c1} r_{c2} k_0 T_0 B_r F}{P_t G_t G_r L_s G_{sp} \sqrt{N}} SNR} \tag{36}$$

This analysis is based on the minimum target size the system is able to detect in FS mode. Using (36), the minimum detectable sphere radius is estimated. The nanosatellite is set to fly at 400km and 600km, and all three illuminators are considered for two scenarios with fixed SNR at 0dB and 10dB respectively. Fig. 11, shows the minimum radius of a sphere which can be detected at a specific altitude and fixed SNR, in FS. From Fig. 11, the system is able to detect spheres down to a few centimetres in radius whereas, depending on the receiver altitude and the required SNR, the detection performance changes accordingly. Furthermore, the impact on the baseline length is noticeable since smaller targets can be detected exploiting illuminators with relative lower altitude or setting the receiver at higher altitude and therefore, be closer to the transmitter. From Fig. 11b, it is noticed that even with 10dBs of required SNR the system can detect spheres down to 2-6cm on average radius for all target altitudes.

5 Simulation Results

In this section results based on simulated data are presented. First, the model validation is presented by comparing the FS true analytical signal in (3), with the SISAR signal model developed in (21). Four different object shapes are considered for this analysis, a rectangle, triangle, circular and a more complex shape target, shown in Fig. 13 where the shadow profiles are plotted. The maximum dimension of each target is set not larger than 2m. Fig. 14, illustrates the envelopes and the normalized phase difference, between the theoretical and ME-SISAR signal models, of all target profiles. The HY2A illuminator is chosen for this simulation and the receiver and target are set to 400km and 700km respectively. From Fig. 14 it can be observed that the ME-SISAR model fits the theoretical signal model well. The error appearing in the phase of the ME-SISAR model in all

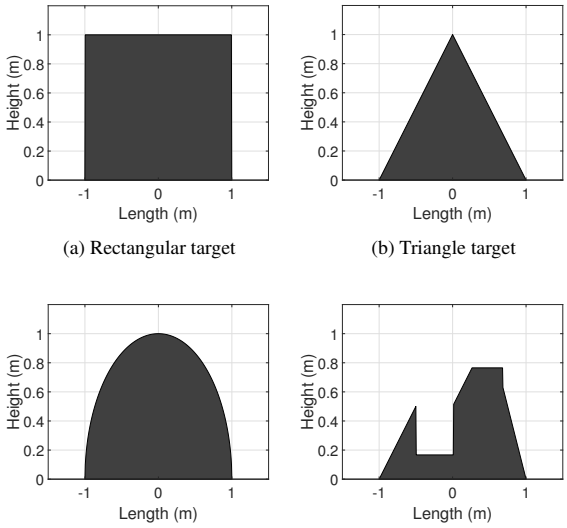

(a) Rectangular target (b) Triangle target

(c) Circular target (d) Complex shape target

Fig. 13: Target profiles

cases is due to the approximations in both distances variables in (6) and (7) as well as in the CPF integral approximation in (13). However, the impact of the error on the model can be omitted due to its occurrence on the zero crossings of the signal's envelope. In Fig. 15, the output of SISAR imaging is shown for all four objects. Depending on the geometry parameters, the resolution of the system varies. However, the final image output is very similar to the target shadow profile and it can be used directly as an input to a classifier. In Fig. 16, the SISAR output is investigated under noisy environment. The received signal is simulated considering different values of SNR and the SISAR output is plotted for every target shape. From Fig. 16, one can see that ME-SISAR algorithm works well under noise since even for low SNR values, down to -10dB, the final output fits well the target's true profile without deviating from the target's shape. For SNR values below -10dB, the final image starts to highly deviate from the true target profile. The performance of this algorithm under noise is assessed in the classification section followed. Except from the noise, another important factor for the algorithm performance, is the target motion estimation errors. Large estimation errors can lead to poor SISAR imaging as well as to a total algorithm failure. In Fig. 17 and 18, the impact of altitude and inclination angle estimation errors are plotted for different estimation errors. Altitude estimation errors do not affect the output shape significantly. From Fig. 17, one can see that even for altitude estimation errors up to 200m, the SISAR output adequately fits the target profile while the algorithm can totally fail for altitude estimation errors above 2km. In contrast with altitude errors, as shown in Fig. 18, the impact of inclination angle on the SISAR final output is significant. The algorithm can

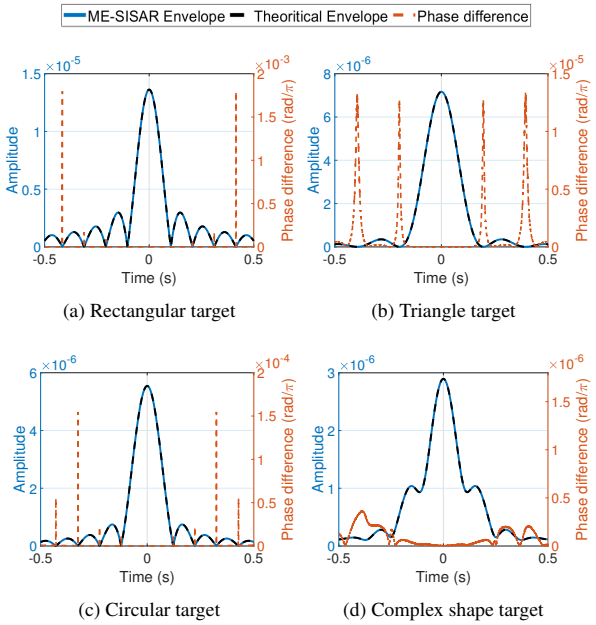

(a) Rectangular target (b) Triangle target

(c) Circular target (d) Complex shape target

Fig. 14: Envelope and phase difference diagrams

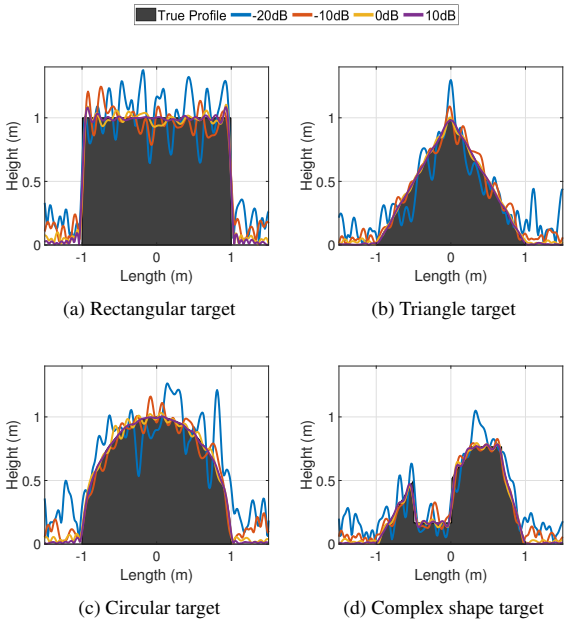

(a) Rectangular target (b) Triangle target

(c) Circular target (d) Complex shape target

Fig. 16: SISAR output for different SNR

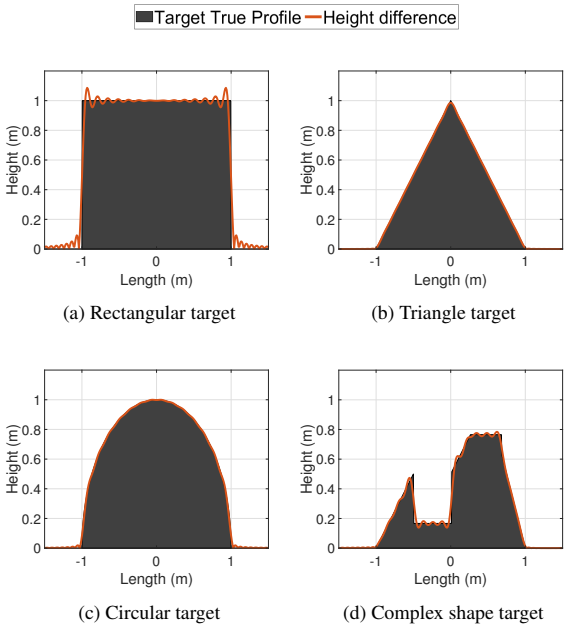

(a) Rectangular target (b) Triangle target

(c) Circular target (d) Complex shape target

Fig. 15: SISAR output

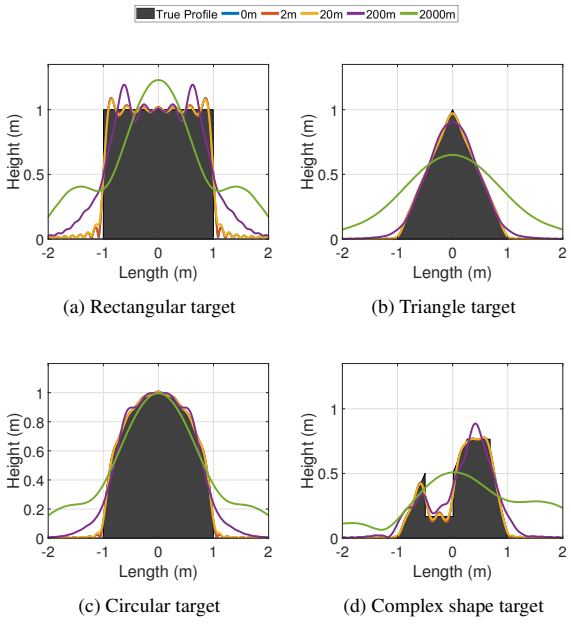

(a) Rectangular target (b) Triangle target

(c) Circular target (d) Complex shape target

Fig. 17: SISAR output for different altitude estimation error

fail for small inclination angle estimation error above 3^o. Therefore, SISAR output performance relies the most on the correct inclination angle estimation and it is less sensitive on the correct altitude estimation.

5.1 Classification

As previously mentioned, the output of the SISAR algorithm is very similar to the target projected shadow profile and therefore, it can be used directly as a vector feature to input a classifier. In this section, an analysis using simulated data is demonstrated using a k-NN classifier. A block diagram of the classification framework is shown in Fig. 12. The received signal is passed through a correlation process to find the target orbital parameters and then, the target height difference can be extracted and fed into a classifier. The two important parameters assessed, are the SNR and the SISAR resolution. These are the major parameters which affect the algorithm performance. Three different target shapes are considered shown in Fig. 13(a)-(c). The complex shape target in Fig. 13(d) is not included in the classification due to its peculiarity and distinctiveness and although it represents a good test bench for the imaging framework, it can bias the classification performance towards higher correct rates. A dataset of 2000 samples for each shape is built for different parameters. Each sample of the dataset is created using a random choice of illuminator listed in Table 1, a random target altitude (in the focusing range

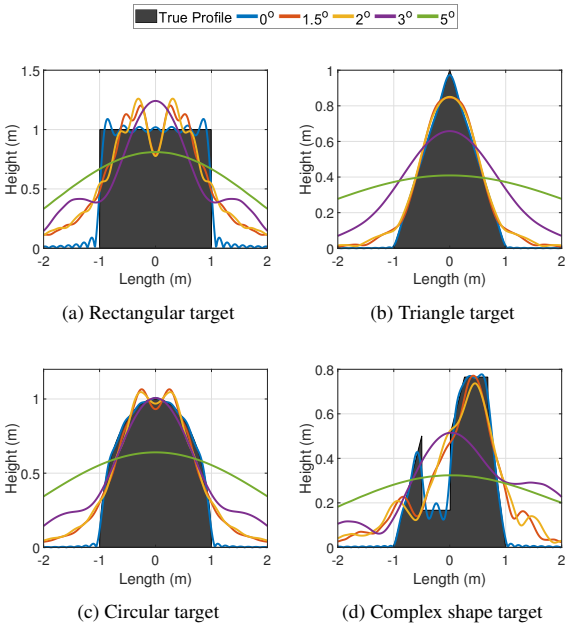

(a) Rectangular target (b) Triangle target

(c) Circular target (d) Complex shape target

Fig. 18: SISAR output for different inclination angle estimation error

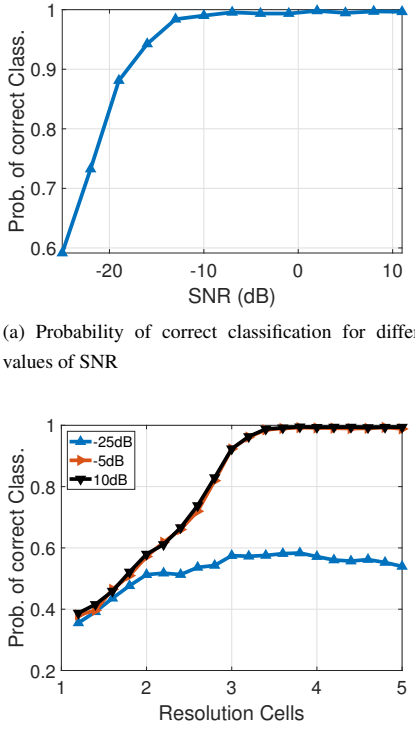

(a) Probability of correct classification for different values of SNR

(b) Probability of correct classification for different values of system resolution

Fig. 19: Probability of correct classification using kNN classifier

700km-900km) and inclination angle, a random SNR value for the received FS signal, target length D between $0.15 - 2$m and receiver altitude between $400 - 600$km. In Fig. 19a, the probability of correct classification is plotted for different values of the received FS signal SNR. The observation time for each iteration is calculated depending on the target size, FSML, target altitude and inclination angle. It can be seen from Fig. 19a that the system can classify between these three shapes quite well with accuracy above 90% for SNR values above $-15dB$. In Fig. 19b, the impact of the system resolution is assessed for different values of SNR. It is obvious that system resolution is an important factor for target classification. From Fig. 19b, the probability of correct classification becomes higher than 95% for resolution less than one third of target length and for SNR higher than -10dB. Therefore, the system resolution limits the performance of this algorithm.

6 Conclusion

In this paper a novel model for SISAR imaging using passive nanosatellites for space debris was presented. The signal model is based on the Fresnel-Kirchhoff diffraction formula and receiver and transmitter moving directions taken into consideration. Through simulation results the algorithm performance was assessed in terms of the system resolution achieved for different target parameters such as size, altitude and inclination angle. System resolution is highly dependent on the target inclination angle relative to both transmitter and receiver whereas, the impact of the altitude of the target does not significantly affect the number of resolution cells acquired.

From the simulated results, was shown that the SISAR model fits the true FS signal of the target with some phase errors due to the CPF integral and distance variables approximations. Furthermore, the relationship between the observation time and target size was analysed in detail. It was shown that relatively smaller targets may enhance integration time due to their wider FSML width and therefore, even smaller target silhouettes can be extracted by dynamically choosing integration time. However, this imaging algorithm depends heavily on the successful estimate of the target motion parameters. A method based on a bank of matched filters was proposed in this paper estimating both target altitude and inclination angle. However, a more detailed analysis of target orbital parameters estimation is omitted since it is not under the scope of this paper. Finally, exploiting the output of the SISAR algorithm, a classification scheme was applied to discriminate between simple target shapes which shows promising results. Future work will investigate the validation of this algorithm and signal model using experimental data.

7 References

1 ESA, "About space debris," 2009. [Online]. Available: https://www.esa.int/Our_Activities/Space_Safety/Space_Debris/About_space_debris

2 ESAmultimedia, 2019. [Online]. Available: http://esamultimedia.esa.int/multimedia/publications/Space_Debris/

3 NASA, 2019. [Online]. Available: https://www.nasa.gov/centers/wstf/site_tour/remote_hypervelocity_test_laboratory/micrometeoroid_and_orbital_debris.html

4 J. Ender, L. Leushacke, A. Brenner, and H. Wilden, "Radar techniques for space situational awareness," in *2011 12th International Radar Symposium (IRS)*, Sep. 2011, pp. 21–26.

5 J. Markkanen, M. Lehtinen, and M. Landgraf, "Real-time space debris monitoring with eiscat," *Advances in Space Research*, vol. 35, no. 7, pp. 1197 – 1209, 2005, space Debris.

6 2019. [Online]. Available: https://www.esa.int/Our_Activities/Space_Safety/Space_Debris/Scanning_and_observing2

7 C. R. Benson, "Enhancing space situational awareness using passive radar from space based emitters of opportunity," in *2014 Military Communications and Information Systems Conference (MilCIS)*, Nov 2014, pp. 1–5.

8 A. R. Persico, P. Kirkland, C. Clemente, J. J. Soraghan, and M. Vasile, "Cubesat-based passive bistatic radar for space situational awareness: A feasibility study," *IEEE Transactions on Aerospace and Electronic Systems*, vol. 55, no. 1, pp. 476–485, Feb 2019.

9 I. Theodorou, C. Clemente, and M. Vasile, "A passive debris tracking system in support to future space traffic management," in *15th Reinventing Space Conference, Glasgow, UK*, October 2017.

10 S. Tao, S. Xiuming, and C. Jing, "Three-dimensional imaging of spinning space debris based on the narrow-band radar," *IEEE Geoscience and Remote Sensing Letters*, vol. 11, no. 6, pp. 1041–1045, June 2014.

11 X. Bai, F. Zhou, M. Xing, and Z. Bao, "Scaling the 3-d image of spinning space debris via bistatic inverse synthetic aperture radar," *IEEE Geoscience and Remote Sensing Letters*, vol. 7, no. 3, pp. 430–434, July 2010.

12 J. Zhu, S. Zhu, and G. Liao, "High-resolution radar imaging of space debris based on sparse representation," *IEEE Geoscience and Remote Sensing Letters*, vol. 12,

no. 10, pp. 2090–2094, Oct 2015.
13 Y. Ning, F. Zhou, X. Bai, and L. Liu, "A method for 3-d isar imaging of space debris," *IEEE Transactions on Aerospace and Electronic Systems*, vol. 55, no. 2, pp. 864–876, April 2019.
14 S. Zhang, Y. Liu, and X. Li, "Bayesian Bistatic ISAR Imaging for Targets with Complex Motion under Low SNR Condition," *IEEE Transactions on Image Processing*, 2018.
15 S. Zhang, Y. Liu, X. Li, and G. Bi, "Joint Sparse Aperture ISAR Autofocusing and Scaling via Modified Newton Method-Based Variational Bayesian Inference," *IEEE Transactions on Geoscience and Remote Sensing*, 2019.
16 V. V. Chapurskiy and V. N. Sablin, "Sisar: shadow inverse synthetic aperture radiolocation," in *Record of the IEEE 2000 International Radar Conference [Cat. No. 00CH37037]*, May 2000, pp. 322–328.
17 I. Theodorou, C. V. Ilioudis, C. Clemente, and M. Vasile, "Sisar imaging - radio holography signal reconstruction based on receiver-transmitter motion," in *2019 IEEE Radar Conference (RadarConf)*, April 2019, pp. 1–6.
18 C. V. Ilioudis, J. Cao, I. Theodorou, P. Striano, W. Coventry, C. Clemente, and J. Soraghan, "Gnss based passive radar for uav monitoring," in *2019 IEEE Radar Conference (RadarConf)*, April 2019, pp. 1–6.
19 M. A. Richards, J. A. Scheer, and W. A. Holm, *Principles of modern radar: Basic principles*, 2010.
20 M. E. Cherniakov, *Bistatic Radar: Principles and Practice*, 2007.
21 M. Gashinova, L. Daniel, E. Hoare, V. Sizov, K. Kabakchiev, and M. Cherniakov, "Signal characterisation and processing in the forward scatter mode of bistatic passive coherent location," *EURASIP Journal on Advances in Signal Processing*, vol. 2013, 12 2013.
22 E. W. Max B, *Principles of Optics*, 1999.
23 NASA, "Report to the united nations office 2011." [Online]. Available: https://www.wikiwand.com/en/Space_debris
24 2019. [Online]. Available: https://directory.eoportal.org/web/eoportal/satellite-missions/h/hy-2a
25 2019. [Online]. Available: https://directory.eoportal.org/web/eoportal/satellite-missions/j/jason-3
26 2019. [Online]. Available: https://gsproductsupport.files.wordpress.com/2009/04/description-of-the-globalstar-system-gs-tr-94-0001-rev-e-2000-12-07.pdf
27 C. Hu, M. Antoniou, M. Cherniakov, and V. Sizov, "Quasi-optimal signal processing in ground forward scattering radar," *2008 IEEE Radar Conference, RADAR 2008*, pp. 1–6, 2008.
28 N. Ustalli, P. Lombardo, and D. Pastina, "Detection performance of a forward scatter radar using a crystal video detector," *IEEE Transactions on Aerospace and Electronic Systems*, vol. 54, no. 3, pp. 1093–1114, June 2018.
29 M. Cherniakov, M. Gashinova, L. Daniel, V. Sizov, and E. Hoare, "Phenomenology of Doppler forward scatter radar for surface targets observation," *IET Radar, Sonar & Navigation*, vol. 7, no. 4, pp. 422–432, 2013.
30 Y. Rahmat-Samii, V. Manohar, and J. M. Kovitz, "For satellites, think small, dream big: A review of recent antenna developments for cubesats." *IEEE Antennas and Propagation Magazine*, vol. 59, no. 2, pp. 22–30, April 2017.
31 "Composite Technology Development, Inc." [Online]. Available: https://www.ctd-materials.com/engineered-materials/tembo/
32 "Ultra-Compact Ka-Band Parabolic Deployable Antenna (KaPDA) for Cubesats," 2014. [Online]. Available: https://icubesat.files.wordpress.com/2014/06/icubesat-org_2014_b-1-4-kupda_sauder_20140617.pdf